Energy & Environmental Science

Novel Cu(Zn)-Ge-P compounds as advanced anode materials for Li-ion batteries

Journal:	*Energy & Environmental Science*
Manuscript ID	EE-ART-11-2020-003553.R1
Article Type:	Paper
Date Submitted by the Author:	02-Feb-2021
Complete List of Authors:	Li, Wenwu; Georgia Institute of Technology, School of materials science and engineering; Guangdong University of Technology - University Town Campus, School of materials and energy Shen, Pengfei; Guangdong University of Technology, Guangzhou 510006, PR China, School of Materials and Energy Yang, Lufeng ; Georgia Institute of Technology Chen, Anjie; National Taiwan Normal University, Department of Chemistry Wang, Jeng-Han; National Taiwan Normal University, Department of Chemistry Li, Yunyong; Guangdong University of Technology, School of Materials and Energy Chen, Hailong; Georgia Institute of Technology, School of Mechanical Engineering Liu, Meilin; Georgia Institute of Technology, School of Materials Science and Engineering

Broader context

The ever-growing high-power and energy density requirement for electrical vehicles, huge volume expansion, and relatively expensive raw material hinder the practical application of Ge anodes for rechargeable LIBs, even though it has a volumetric capacity as high as that of Si and, much faster transfer of Li-ion and electron than Si. Multi-phase composites anodes have attracted great attention due to a reversible synergistic effect of the constituent phases of the composites during cycling, thus leading to the improved energy density, cycling life, and rate performance, compared to unary or binary phase materials. Nevertheless, the construction of these complex nanocomposites still faces the great challenge of thermodynamic metastability and sophisticated surface/interface compatibility of the constituent phases of the composites. Therefore, designing rationally multi-phase nanocomposites with superior electrochemical Li-storage performances and low-cost preparation process is of vital importance and great value to the research and development of a new-generation Li-ion battery.

Journal Name ARTICLE

Novel Cu(Zn)-Ge-P compounds as advanced anode materials for Li-ion batteries

Received 00th January 20xx,
Accepted 00th January 20xx

DOI: 10.1039/x0xx00000x

www.rsc.org/

Wenwu Li,*[a,b] Pengfei Shen,[b] Lufeng Yang,[c] Anjie Chen,[d] Jeng-Han Wang,[d] Yunyong Li,[b] Hailong Chen,[c] and Meilin Liu*[a]

Both electronic and ionic conductivity are of high importance to the performances of anode materials for Li-ion batteries. Many large capacity anode materials (such as Ge) do not have sufficiently high electronic and ionic conductivity required for high-rate cycling. Here we report a novel ternary compound copper germanium phosphide ($CuGe_2P_3$) as a high-rate anode. Synthesized via a facile and scalable mechanochemistry method, $CuGe_2P_3$ has a cation-disordered sphalerite structure and offers higher ionic and electronic conductivities and better tolerance to volume change during cycling than Ge, as confirmed by first principles calculations and experimental characterization, including high-resolution synchrotron X-ray diffraction, HRTEM, SAED, XPS and Raman spectroscopy. Further, results suggest that $CuGe_2P_3$ has a reversible Li-storage mechanism of conversion reaction. When composited with graphite by virtue of a two-stage ball-milling process, the yolk-shell structure of amorphous carbon-coated $CuGe_2P_3$ nanocomposite ($CuGe_2P_3$/C@Graphene) delivers high initial Coulombic efficiency (91%), superior cycling stability (1,312 mA h g^{-1} capacity after 600 cycles at 0.2 A g^{-1} and 876 mA h g^{-1} capacity after 1,600 cycles at 2 A g^{-1}), and excellent rate capability (386 mA h g^{-1} capacity at 30 A g^{-1}), surpassing most Ge-based anodes reported to date. Moreover, a series of cation-disordered new phases in the Cu(Zn)-Ge-P family with various cation ratios offer similar Li-storage properties, achieving high reversible capacities with high initial Coulombic efficiency and desirable redox chemistry with improved safety.

Introduction

Lithium-ion batteries (LIBs) have attracted extraordinary attention for many emerging applications, from portable devices to electric vehicles. However, the existing LIBs are still unable to meet the ever-increasing demands, and further improvement is needed to achieve higher gravimetric and volumetric energy densities and longer service life. Electrode materials based on alloy-type reactions are often able to accommodate several Li ions and electrons per host atom, offering high capacity. In particular, Si, Ge, and binary Si_xGe_{1-x} alloys are regarded as potential alternatives to the widely used graphite anodes, due largely to their rather large Li-storage capacity (3,578 mA h g^{-1} capacity for $Li_{15}Si_4$ and 1,385 mA h g^{-1} capacity for $Li_{3.75}Ge$). The high volumetric capacities (9,781 and 8,645 mA h cm^{-3} for Si and Ge anodes, respectively, compared with graphite of 790 mA h cm^{-3}) also represent a significant advantage. Although Ge has greater electronic and Li-ionic conductivity than Si counterparts[1-4], the inherent electronic and Li-ionic conductivity still needs to be significantly enhanced to achieve ultrahigh rate performance. In addition, the large volume variation during cycling usually results in growth of variable solid electrolyte interphase (SEI) films as well as in a severe electronic contact loss of electrodes, thus leading to relatively low initial Coulombic efficiency and fast capacity decay.[5]

To overcome the above challenges while simultaneously enhancing Li-storage performances of alloy anode materials, various advanced nanostructures have been studied.[6-14] Nanosizing was demonstrated to be an effective strategy to the issues associated with extensive volume change. The open space within these nanostructures effectively accommodates the volume changes of the alloy-type anode materials during cycling, thus delaying the eventual capacity decay. However, most of these strategies require rather complex synthesis methods. Also, nanosizing inevitably decreases the tapping density and hence volumetric capacity of the electrode. Therefore, it is critical to keep a high packing density of the active material particles while ensuring an efficient electronic and ionic conduction throughout the electrode.

To significantly enhance inherent electronic and Li-ionic conductivity of Ge, researchers resorted to atomic substitution or doping[15-24] in searching for new binary[25-29] and ternary Ge-based anode materials[30-34]. For example, Se-doped Ge microparticles with high tap density achieved high-rate performance and long cycling stability of over 1,000 cycles, profiting from not only the significantly improved electronic and Li-ionic conductivities but also the formed highly Li-permeable amorphous Li-Ge-Se inactive phase during cycling, which is responsible for alleviating strain and enhancing Li-ionic diffusion rate.[16] The ternary metal germanium oxides/chalcogenides are attractive for electrochemical energy storage applications since there exist possible synergistic effect of the electroactive multi-components endowed by their outstanding physical, chemical, thermal and electronic properties.[35-38] More interestingly, Si-doped ternary Zn_2GeO_4 compound effectively suppress volume change, thus demonstrating a large capacity of 1,274 mA h g^{-1} at 200 mA g^{-1}

[a] School of Materials Science & Engineering, Georgia Institute of Technology, Atlanta, GA, 30332, USA.
[b] School of Materials and Energy, Guangdong University of Technology, Guangzhou, 510006, PR China.
[c] The Woodruff school of Mechanical Engineering, Georgia Institute of Technology, 771 Ferst Drive, Atlanta, GA, 30332, USA.
[d] Department of Chemistry, National Taiwan Normal University, Taipei, 11677, Taiwan.
*Corresponding authors, E-mail:wenwuli@gdut.edu.cn; meilin.liu@mse.gatech.edu
Electronic Supplementary Information (ESI) available: details of any supplementary information available should be included here]. See DOI: 10.1039/x0xx00000x

after 700 cycles as well as robust cycle stability of 2,000 cycles at 5 A g^{-1} with a capacity decay ratio of 0.008% per cycle. The excellent performances mainly benefit from the substitution of Si atom. Such substitution imparts to Zn_2GeO_4 compound both high reactivity and reversibility as well as stress-relieved merits during discharge, as validated by virtue of first-principles calculations.[37] Unfortunately, the above ternary materials present compromised Li-storage performances because electrochemically derived products usually differ from each other in working potentials, thus showing a multi-stage redox chemistry. Moreover, most capacity contributions of ternary metal germanium oxides and sulfides are corresponded to the working potentials above 1.0 V, thus leading to relatively low energy density. Compared with oxides/chalcogenides, phosphides have higher energy efficiency and larger theoretical reversible capacity benefiting from lower formation energy of Li_3P compared with Li_2O.[39,40] Nevertheless, to our best knowledge, there is no ternary metal germanium phosphides reported for electrochemical energy-storage since it is quite challenging to synthesize these ternary metal germanium phosphides by a facile method resulting from their thermodynamic meta-stability. Thus, designing metal germanium phosphides rationally with right chemistry as well as appropriate working potentials needs fundamental insights into structure-performance relationship, which is of urgence and vital importance to the research and development for a new battery technology.

Here we report the successful co-integration of Cu and P into Ge to synthesize a novel ternary copper germanium phosphide of $CuGe_2P_3$. High-resolution synchrotron X-ray diffraction (XRD) and refinement, and first-principles calculations demonstrate the as-synthesized $CuGe_2P_3$ features cation-disorder and has faster electronic and Li-ionic conductivities, and greater tolerance against volume variation, compared with Ge counterparts. As anode of LIBs, the as-synthesized $CuGe_2P_3$ offers a large reversible capacity of 1,457 mA h g^{-1} with an initial Coulombic efficiency up to 92% and a reasonable working potential of 0.5 V based on a reversible Li-storage mechanism of conversion reactions, as confirmed by various characterizations and electrochemical measurements. After a two-stage ball milling $CuGe_2P_3$ with graphite, $CuGe_2P_3$/C@Graphene shows a long cycling stability (1,312 mA h g^{-1} capacity after 600 cycles at 200 mA g^{-1}, and 876 mA h g^{-1} capacity after 1,600 cycles at 2 A g^{-1}), an ultrahigh rate performance (386 mA h g^{-1} capacity at 30 A g^{-1}). Further, we extend $CuGe_2P_3$ into a novel series of cation-disordered Cu(Zn)-Ge-P compounds with a large range of cationic ratios, which also present large capacities with high initial Coulombic efficiency and suitable working potentials, thus further demonstrating their high promise as the next-generation high-performance anode materials for LIBs.

Results and Discussion

The complete Si-Ge solid solution with Ge-like atomic arrangement[20-24] wins significantly superior Li-storage performances to the related single-component Ge anodes. Broadly, $A^{II}B^{IV}C_2^{V}$ and $A^{I}B_2^{IV}C_3^{V}$ compounds with a wide range of valences also own similar crystal structure. However, their Li-storage performances are rarely reported due to complex synthetic conditions. Herein, we have obtained $CuGe_2P_3$ by means of a simple and scalable mechanical ball milling method at room temperature under atmospheric pressure, thus saving the traditional chemical vapor transportation technique at high-temperature and high-pressure[29-31]. The synthetic process is schematically illustrated in **Fig. 1a**. To track the synthetic process, we collect the intermediate products at a predetermined ball milling time. As shown in **Fig. 1b,** after milling for 10 min, the fingerprint diffraction peaks for the raw materials of Cu, amorphous red P, and Ge still co-existed; at 0.5 h, the diffraction peaks of Cu and amorphous red P disappeared; at 2 h, a ternary phosphide of $CuGe_2P_3$ appeared regardless of the residual Ge. After milling of 10 h or longer, we obtained the pure $CuGe_2P_3$ with Ge-like XRD pattern. To determine the structural parameters of the newly synthesized phase, we resorted to the XRD refinement (**Fig. 1c**) of the as-synthesized $CuGe_2P_3$. As depicted in **Fig. 1a**, the model cell can be well-assigned to cation-disordered sphalerite structure, where Cu and Ge replace Zn site randomly in the given mole ratio of 1:2 and P occupies S site completely. Detailed crystallographic data are given in **Table S1-Table S2**. Furthermore, the cation-disordered crystal structure of the sample was characterized by high-resolution synchrotron X-ray diffraction (**Fig. 1b**, **top** and **Table S3**); the results suggest that no impure phases were detected after milling for 10 h, with the only phase being the newly synthesized cation-disordered $CuGe_2P_3$. To observe the detailed morphology, we performed field-emission scanning emission microscopy (FESEM) and low-magnification transmission electron microscopy (TEM) measurements. As shown in **Fig. S1**, the $CuGe_2P_3$ sample is composed of microsized secondary particles, which are consisting of numerous aggregated primary nanoparticles. To precisely control the particle size or morphology, the ternary Cu-Ge-P compounds may be synthesized by the phosphization of the ternary Cu-Ge-O compounds with different morphologies. The Cu-Ge-P compounds may also be synthesized using a wet chemical method such as solvothermal reaction of copper salts, germanium salts or oxides and organic phosphorus sources. To probe more detailed information on the micro-structure, we further characterized the as-synthesized $CuGe_2P_3$ using high-resolution transmission electron microscopy (HRTEM, **Fig. 1e**), including selected area electron diffraction (SAED, the inset in the **Fig. 1e**). The measured zonal facets of $(2\bar{2}0)$ and (220) along the [001] zone axis as well as no observed diffraction rings associated with the cation-ordered superstructure further validate the cation-disordered sphalerite structure of the as-synthesized $CuGe_2P_3$. Additionally, the common Ge-like crystal plane of (111) is also observed as presented in **Fig. S2**. In addition, we also characterized Raman spectra of the cation-disordered $CuGe_2P_3$. As shown in **Fig. 1d** and **Fig. S3**, its fingerprint peaks are completely different from those of the ball milled Ge and P, thus suggesting the formation of ternary $CuGe_2P_3$.

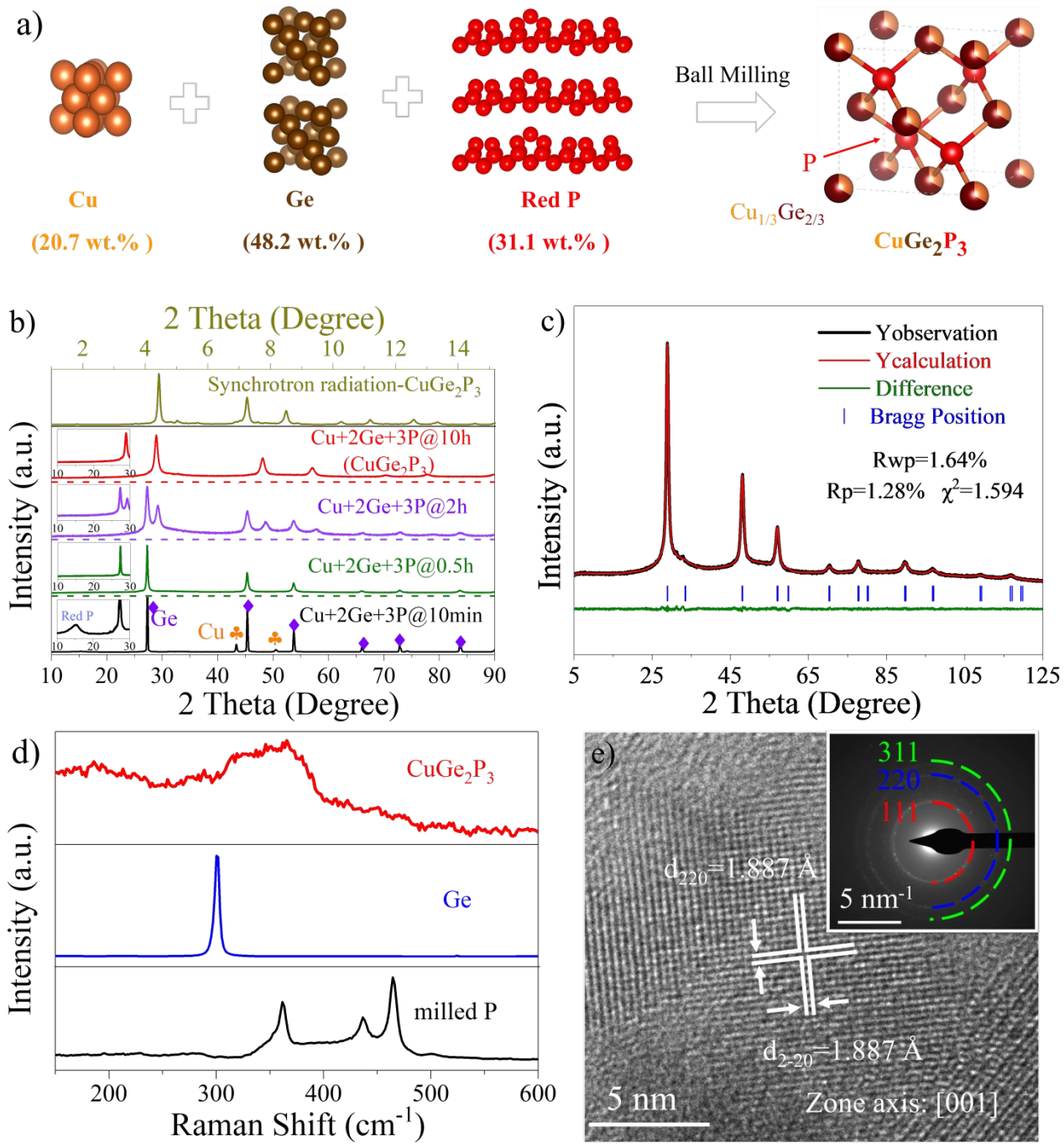

Fig. 1. (a) Schematically illustrated preparation procedure of the cation-disordered $CuGe_2P_3$ compound; (b) evolved X-ray diffraction patterns (XRD) of Cu+2Ge+3P samples (Cu+2Ge+3P@x h means milling at x h , x =1/6, 0.5, 2, 10); (c) XRD refinement of the above synthesized Cu+2Ge+3P@10h sample; (d) Raman spectroscopy of the above-synthesized cation-disordered $CuGe_2P_3$ sample, milled P and Ge powders; (e) high-resolution transmission electron microscopy (HRTEM) image along with selected area electron diffraction (SAED; the inset at top right) pattern of the above-synthesized cation-disordered $CuGe_2P_3$.

Encouraged by the cation-disordered structure and Li-storage components of Ge and P, we believe that the as-prepared ternary metal germanium phosphide of $CuGe_2P_3$ would offer unparalleled Li-storage properties, compared with the single-component and binary compounds anodes. The electrochemical Li-storage performances of the Cu+2Ge+3P samples corresponded to the above-analyzed XRD data as well as the milled Ge and P samples were evaluated. As compared in **Fig. 2a**, **Fig. 2b** and **Fig. 2d**, the pure $CuGe_2P_3$ shows the best Li-storage properties in terms of suitable working potential, small polarization loss, large reversible specific capacity and high initial Coulombic efficiency. Specifically, the as-synthesized $CuGe_2P_3$ shows a reversible capacity of 1,457 mA h g^{-1} with an initial Coulombic efficiency up to 92%, and a suitable working

potential of 0.5 V. It should be noted that although the intermediate Cu+2Ge+3P samples deliver obvious multi-stage Li-storage properties, the as-synthesized $CuGe_2P_3$ shows relative smooth discharge-charge profiles, which favors the discharge depth control when applied in full cells. This phenomenon can be probably attributed to different electrochemical Li-storage process caused by the primary micro-structural difference of these materials. **Fig. 2c** and **Fig. S4a-4b** shows the initial cyclic voltammetry curves of the as-synthesized $CuGe_2P_3$, which are well-consistent with the redox potentials delivered by the initial discharge-charge profiles. During the first reduction process, there exist two reduction bands centered at 0.547 V and 0.183 V (vs. Li^+/Li), which can be explained as a small amount of side reaction such as the formation of solid electrolyte interphase and then the Li-ionic uptake reaction of $CuGe_2P_3$. During the oxidation process, there exist three oxidation peaks locating at 0.491 V, 0.861 V and 1.156 V, corresponded to Li-ionic extraction of binary Li-Ge, Li-P alloys and $Li_xCuGe_2P_3$, respectively. During the subsequent reduction process, there exist three reduction peaks centered at 0.7 V, 0.5 V and 0.16 V, corresponded to the Li-ionic uptake and formation of $Li_xCuGe_2P_3$ as well as binary Li-P and Li-Ge alloys. Compared with the initial cycle, the subsequent cycles obtain the slightly reduced polarization, which mainly result from defects produced during the first discharge-charge process, leading to faster Li-ionic and electronic conductivity. It should be noted that compared with some P-based anodes, the $CuGe_2P_3$ presents relatively low working potential, which may be attributed to the specific structure with different Li-ion diffusion paths and reaction mechanisms.[25,26,41] As observed in **Fig. 2d** and **Fig. S4c**, the as-synthesized $CuGe_2P_3$ delivers a large reversible capacity of 1,457 mA h g^{-1} at 100 mA g^{-1} and can be cycled over 100 cycles without obvious decay, which is superior to other impure Cu+2Ge+3P samples as well as the milled Ge and P electrodes. Moreover, $CuGe_2P_3$ shows significantly improved rate performance (**Fig. 2e**), compared with milled Ge anodes. Even, when cycled without any conductive agent, $CuGe_2P_3$ can still deliver a large reversible capacity of 1,260 mA h g^{-1} with an initial Coulombic efficiency up to 90% at 100 mA g^{-1} (**Fig. S5**). The significantly enhanced rate capability of the as-prepared $CuGe_2P_3$ anodes can be probably assigned to its much quicker Li-ionic and electronic transport kinetics compared with the Cu+2Ge+3P and Ge samples, which will be analyzed below.

Considering the as-synthesized $CuGe_2P_3$ as a promising anode material for LIBs with superior electrochemical Li-storage performances in respect of large reversible capacity, high initial Coulombic efficiency, high-rate performance and high energy efficiency, we further performed the ex-situ high-resolution synchrotron X-ray diffraction, XRD, HRTEM along with SAED and FFT, Raman and XPS to characterize its structural evolution during discharge-charge process. As shown in **Fig. S6**, the crystal structure of the $CuGe_2P_3$ owns enough space to accommodate up to three Li-ions within the tetrahedral sties surrounded by the occupied cationic and anionic sites in the sphalerite structure. As shown in **Fig. S7** and **Fig. S8**, the energies associated with insertion of Li ions into $CuGe_2P_3$ to form $LixCuGe_2P_3$ (x=1/16 to 3) are all negative, confirming the probability of forming the $LixCuGe_2P_3$ (x<3) phases during lithiation. As presented in **Fig. 3a** and **Fig. 3b$_1$-Fig. 3b$_2$**, with the decreasing potential, the $CuGe_2P_3$ began to uptake Li-ions indicated by its gradual amorphization, where the XRD pattern features as no diffraction peaks. As continued lithiation, the amorphous electrode became crystallize Li_2CuP and other amorphous products. We noted the crystallize Li_2CuP compound owns both Li-ionic and electronic conductivities[42], simultaneously, which helps to achieve ultrahigh rate performances. When completely discharged to 5 mV, the electrode degraded into the almost amorphous mixture of Li_3P, $Li_{3.75}Ge$ and Cu as co-confirmed by XRD (**Fig. 3b$_5$**), the ex-situ Raman (**Fig. 3c$_4$-Fig. 3c$_6$**), XPS (**Fig. 3d$_3$-3f$_3$, Fig. S10**), ex-situ high-resolution synchrotron X-ray diffraction (**Fig. S11b**) and HRTEM image (**Fig. S12-iii**) along with the corresponding FFT images. Our XPS analysis reveals that, compared with the spectra for the pristine $CuGe_2P_3$ and the mixed powder of Cu, Ge, and P, the peaks of $Li_{15}Ge_4$ (26.95 eV, Fig. 3d$_3$), Li_3P (127 eV, Fig. 3e$_3$), and elemental Cu (932.85 eV, Fig. 3f$_3$) appeared, implying the formation of these lithiation products.[43,44] When charged, the binary Li-M alloys products gradually disappeared and the crystalline Li_2CuP appeared again (**Fig. 3b$_7$** and **Fig. S9**). When completely charged to 3.0 V, the electrode upgraded into almost amorphous $CuGe_2P_3$ as co-validated by Raman (**Fig. 3c$_1$-3c$_2$**, **Fig. 3c$_8$-3c$_9$**), XPS (**Fig. 3d$_4$-3f$_4$, Fig. S10**), the ex-situ XRD (**Fig. 3b9**) and ex-situ high-resolution synchrotron X-ray diffraction (**Fig. S11a-ii**) along with HRTEM and SAED presented in **Fig. S12-v**. It is noted that, compared with the fingerprint XPS signals of pristine crystalline $CuGe_2P_3$, the XPS signals of the amorphous $CuGe_2P_3$ after cycling were shifted slightly to higher binding energy, attributed to the amorphization.[45] It should be also noted that the amorphization of the $CuGe_2P_3$ anodes favors its cycling stability profiting from the uniform strain release during the repeated discharge-charge process.[46] As schematically illustrated in **Fig. 3g**, Li-storage process of $CuGe_2P_3$ is expressed as following equations:

During the Li-ionic uptake process:

$CuGe_2P_3 + x\ Li^+ + x\ e^- \rightarrow Li_xCuGe_2P_3$ (x< 3) (i);

$Li_xCuGe_2P_3 + (16.5\text{-}x)\ Li^+ + (16.5\text{-}x)\ e^- \rightarrow Cu + 2\ Li_{3.75}Ge + 3\ Li_3P$ (ii);

During the Li-ionic extraction process:

$2\ Li_{3.75}Ge + Cu + 3\ Li_3P - (16.5\text{-}x)\ Li^+ - (16.5\text{-}x)\ e^- \rightarrow Li_xCuGe_2P_3$ (iii);

$Li_xCuGe_2P_3 - x\ Li^+ - x\ e^- \rightarrow CuGe_2P_3$ (almost amorphous) (iv);

Total reaction:

$CuGe_2P_3 + 16.5\ Li^+ + 16.5\ e^- \leftrightarrow Cu + 2\ Li_{3.75}Ge + 3\ Li_3P$ (v).

According to the above reaction equations, the $CuGe_2P_3$ electrode can store 16.5 Li-ions per formula unit, contributing to its theoretical capacity of 1,467 mA h g^{-1}, where Ge provides 667 mA h g^{-1}, and P delivers 800 mA h g^{-1}. As known, the electronic conductivity of Cu ranks only second to Au among various metals and thus are widely utilized as current collectors for anode materials of batteries. The endogenous nanoscale Cu during the deep discharge process contributes no capacity, but provides significantly enhanced electronic conductivity and acts as a physical barrier against the electrochemical agglomeration.

Moreover, fast charging always gives rise to the increasing temperatures of operating batteries, the formed Cu, excellent

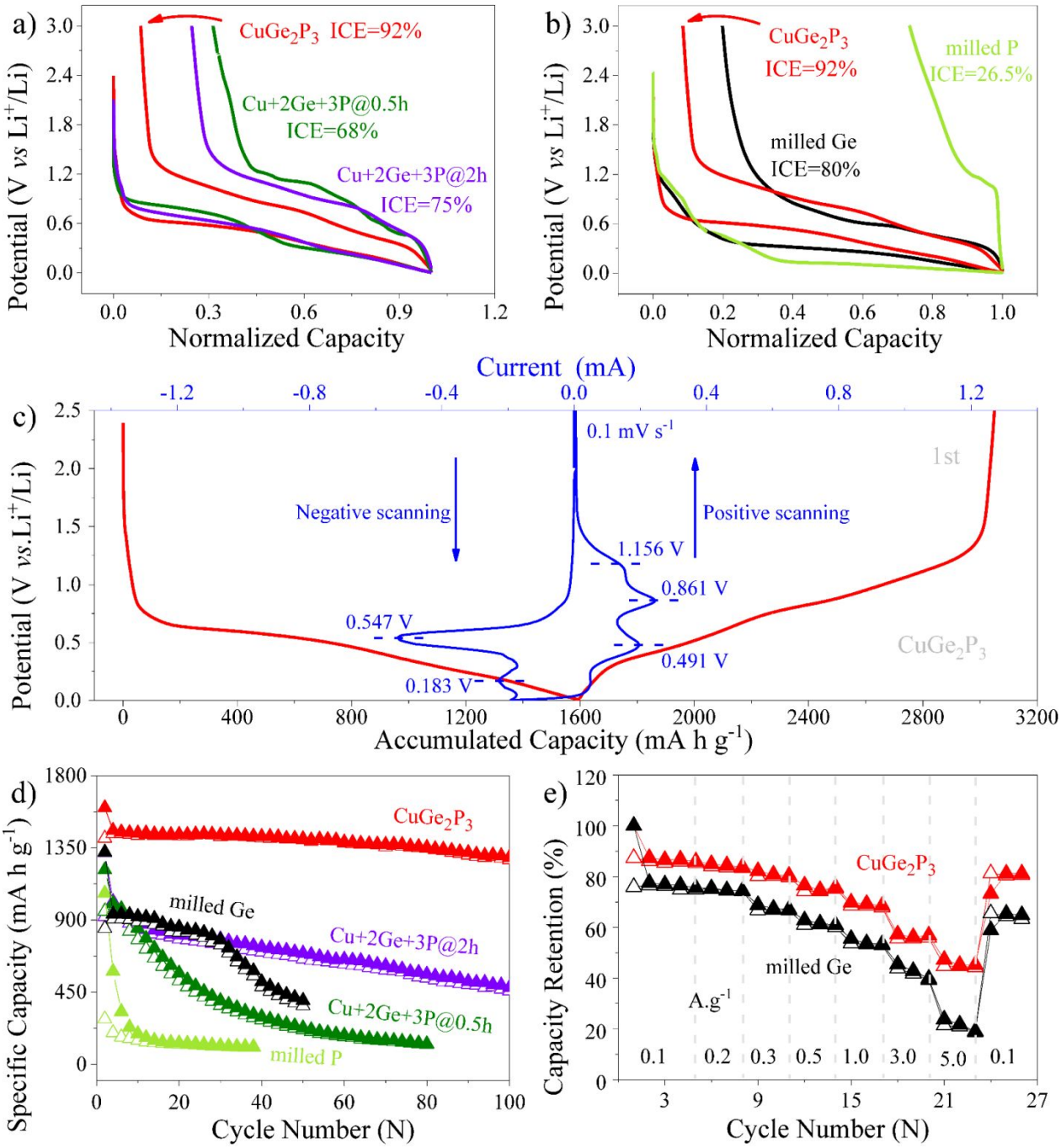

Fig. 2. (a) Initial discharge-charge profiles of the above-synthesized Cu+2Ge+3P samples at various ball-milling time; (b) initial discharge-charge profiles of the above-synthesized cation-disordered $CuGe_2P_3$, milled P as well as milled Ge electrodes; (c) the comparation of initial cyclic voltammetry curves and first galvanostatic discharge-charge profiles for the above synthesized cation-disordered $CuGe_2P_3$ electrodes; (d) cycling stability of the above-synthesized Cu+2Ge+3P samples at various ball-milling time and milled Ge electrodes; (e) rate performance of the as-obtained $CuGe_2P_3$ powder and milled Ge powder.

thermal conductor, will significantly alleviate the local overheating and act as a local thermal protection medium for LIBs.

To find the primary cause behind the superior Li-storage performances of the as-synthesized $CuGe_2P_3$ to Ge counterparts, we performed density functional theory calculations to unveil the Li-ionic and electronic transport kinetics, and resistance capability against volume change. Based on the cation-disordered structural characteristics, we made a recognized cation-disordered model presented in **Fig. S13a**. Firstly, we

calculated the electronic structure of the $CuGe_2P_3$ and Ge. Surprisingly, as presented in **Fig. 4a**, the total DOS value of the cation-disordered $CuGe_2P_3$ crosses the Fermi level, giving the direct evidence for its electronic conductivity. This result is also well-consistent with calculated band structure (**Fig. S14**), which shows no band gap, also suggesting its metallic conductivity. As a comparison, Ge only has a semiconducting feature evidenced by its total DOS value equalling to zero at the Fermi level on the basis of the simulated electronic structure shown in **Fig. 4a**. This calculated result is also well-consistent with literatures published before.[47] The electronic conductivity of the as-prepared $CuGe_2P_3$ can be probably attributed to the cation disorder. To validate DFT calculations results, namely, improved electronic transport kinetic of $CuGe_2P_3$, we carried out electrochemical impedance spectroscopy measurements to obtain charge transfer resistance (R_{ct}) of the $CuGe_2P_3$ anodes. As presented in **Fig. 4b** and **Fig. S15**, the R_{ct} value (72 Ω) of the cation-disordered $CuGe_2P_3$ is significantly smaller than those (172 Ω, 252 Ω and 390 Ω for Ge, Cu+2Ge+3P@2h and Cu+2Ge+3P@0.5h, respectively) of Ge and the ball milled intermediate Cu+2Ge+3P samples, thus validating that the as-synthesized $CuGe_2P_3$ owns best electronic conductivity among

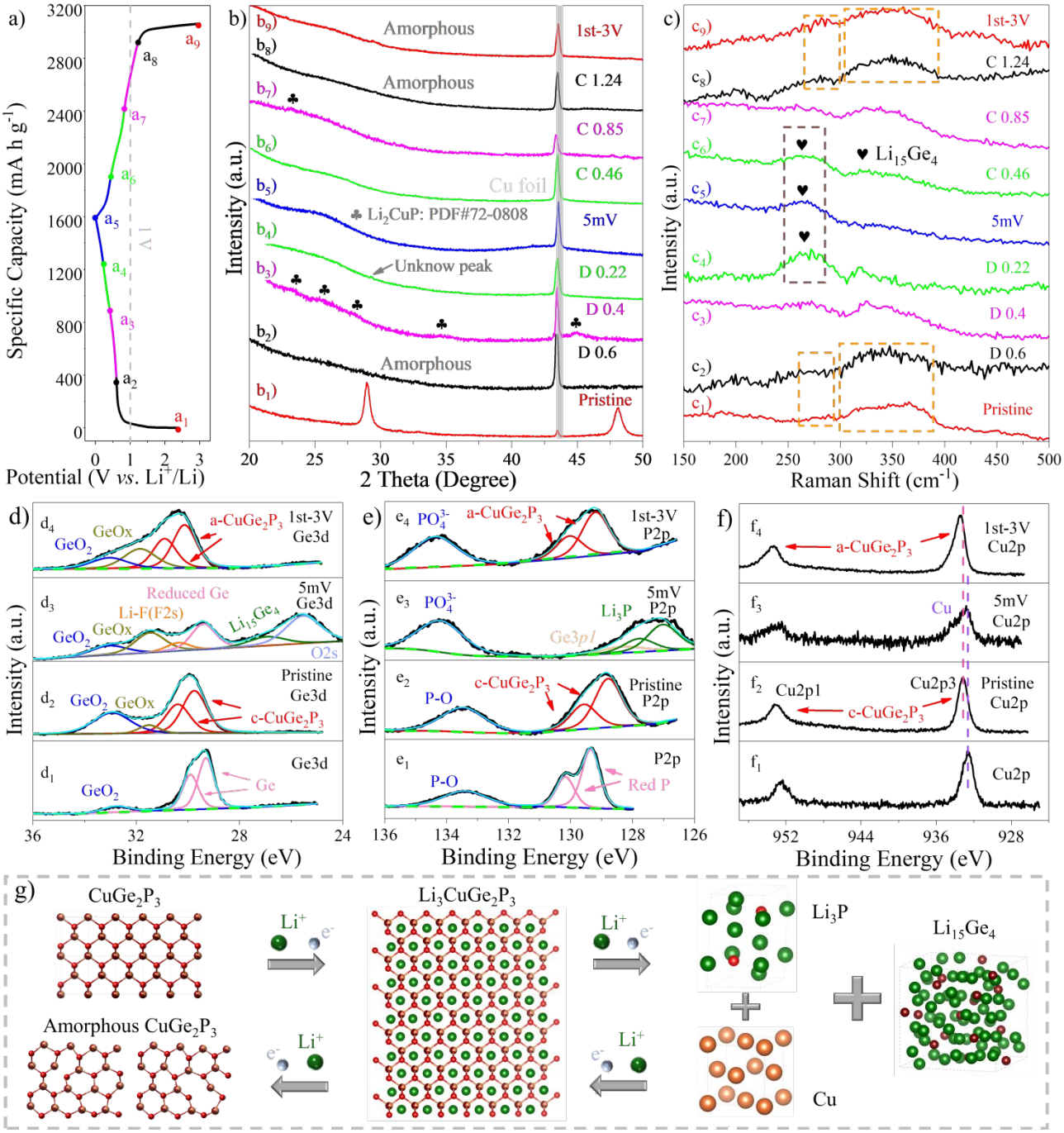

Fig. 3. Li-storage mechanisms characterizations of the $CuGe_2P_3$ anodes: (a) first galvanostatic discharge-charge curves for the ex-situ characterizations at a current rate of 100 mA g^{-1}; (b) ex-situ XRD patterns corresponded to the indicators marked in (a); (c) ex-

situ Raman patterns corresponded to the indicators marked in (a); high resolution XPS spectra of $CuGe_2P_3$ electrode after cycling, pristine $CuGe_2P_3$ powder and raw material of Ge, P or Cu: (d) Ge 3d; (e) P 2p; (f) Cu 2p; (g) scheme of the overall Li-storage process.

these comparisons (Ge and the ball milled Cu+2Ge+3P samples). Moreover, we also measured the electrical conductivity of the $CuGe_2P_3$-based electrodes, the as-synthesized $CuGe_2P_3$ powder, the mixed Cu+2Ge+3P powder, and the raw materials of Ge and P. As shown in **Table S4**, the electrical conductivities of the $CuGe_2P_3$-based electrode and the $CuGe_2P_3$ powder are several orders of magnitude greater than those of the mixed Cu+2Ge+3P powder and the raw materials of Ge and P. Secondly, on Li-ionic storage and diffusion kinetics, we simulated various Li-ionic structural configurations by virtue of filling lithium atoms in the lattices or interstitial sites to optimize the structure featured by the lowest energy. The related lattices were relaxed via applying primary multiple energy minimization calculation principles. As illustrated in **Fig. S6**, there have three voids with enough space to host one Li atom per void, in the crystal structure of the as-synthesized $CuGe_2P_3$. We performed the Li-ionic transport activation energy calculation with a Li-ion hoping among the voids within the random-cation supercell (**Fig. S13**). The Li-ionic diffusion paths follow octahedron-tetrahedron-octahedron sites (**Fig. S16a**) in which every site is encompassed by Ge or Cu atoms. The related Li-ionic transport activation energy barriers are plotted in **Fig. 4d**. Most of the Li-ionic transport activation energy values of the cation-disordered $CuGe_2P_3$ are below 0.26 eV. As a comparison (**Fig. 4d** and **Fig. S16b**), however, most Li-ionic transport activation energies for Ge are over 0.62 eV. The smaller Li-ionic transport barriers of the cation-disordered $CuGe_2P_3$ means its more facile Li-ionic transport kinetic, compared with Ge counterparts. To validate the theoretical predictions, we carried out the galvanostatic intermittent titration measurement to evaluate and compare Li-ionic diffusion capability of the above-synthesized Cu+2Ge+3P samples and Ge electrodes. Li-ionic diffusion coefficients can be determined according to the following equation:

$$D = \frac{4}{\pi}\left(\frac{i\,V_m}{Z^{\wedge}FS}\right)^2\left(\frac{dE/d\sigma}{dE/dt^{\wedge}(1/2)}\right)^2$$

where D corresponds to Li-ionic diffusion coefficient, i represents current, Z_A is Charge number (Z_A=1), F refers to Faraday constant of 96,485 C mol^{-1}, V_m means molar volume of electrodes, S stands for the geometric area of the electrode, dE/dσ is the slope of the coulomtric titration curve, found by plotting the steady state voltages E (V) measured after each titration step σ; and $dE/dt^{\wedge 1/2}$ is the slope of the linearized plot of the potential E (V) during the current pulse of duration t (s). As presented in **Fig. 4e**, **Fig. 4f**, **Fig. S17** and **Fig. S18**, the average Li-ionic diffusion coefficients for the cation-disordered $CuGe_2P_3$

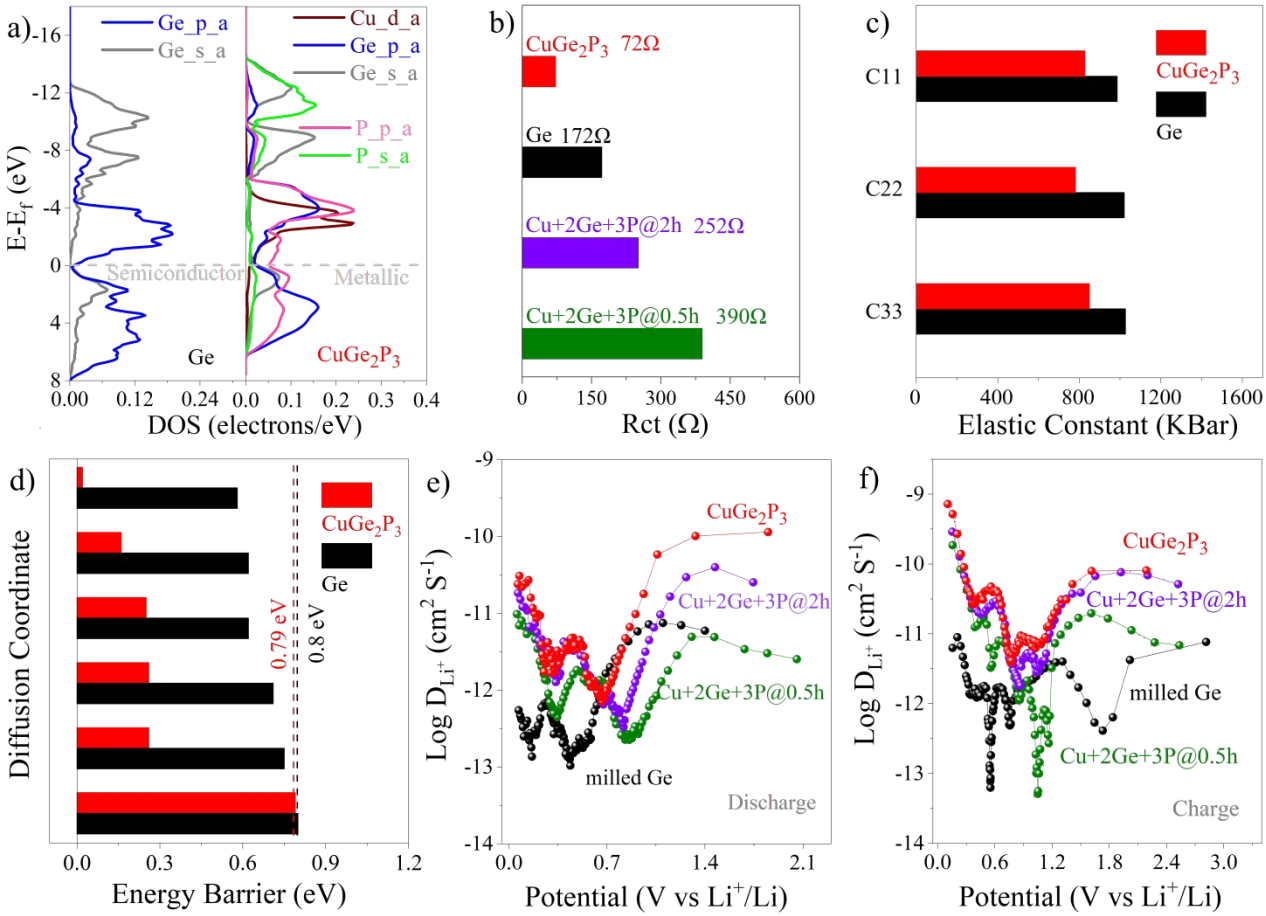

Fig. 4. (a) Density of state (DOS) of $CuGe_2P_3$ and Ge; (b) charge transfer resistance (Rct) of Ge, as well as the above-synthesized Cu+2Ge+3P samples at various ball-milling time; (c) elastic constant of $CuGe_2P_3$ electrode and Ge; (d) diffusion energy barrier of $CuGe_2P_3$ and Ge; Diffusion coefficient of the above-synthesized Cu+2Ge+3P samples at various ball-milling time and milled Ge electrodes; (e) discharge (f) charge.

at the operating potential are faster than the ball milled intermediate Cu+2Ge+3P samples and Ge electrodes counterparts. Thirdly, we calculated the mechanical property of the cation-disordered $CuGe_2P_3$ to evaluate its resistance capability against volume variation during repeated Li-ionic uptake-extraction process utilizing first-principles theory. As compared in **Fig. 4c**, the elastic constants of the as-prepared $CuGe_2P_3$ are significantly smaller than Ge counterparts, which suggests the cation-disordered $CuGe_2P_3$ is much softer than Ge. The softer property means it favors to accommodate the volume variation caused by the repeated lithiation-delithiation of the host material as demonstrated in **Fig. S19**. To make a long story short, the cation-disordered $CuGe_2P_3$ has significantly faster electronic and Li-ionic conductivities (**Fig. 4a** and **Fig. 4d**), as well as stronger resistance to structural change (**Fig. 4c**) compared with Ge counterparts. These calculated results rationalize the Li-storage superiority of the cation-disordered $CuGe_2P_3$ in terms of faster reaction kinetics, smaller polarization loss as well as higher energy efficiency compared with these ball milled intermediate Cu+2Ge+3P samples and Ge electrodes counterparts.

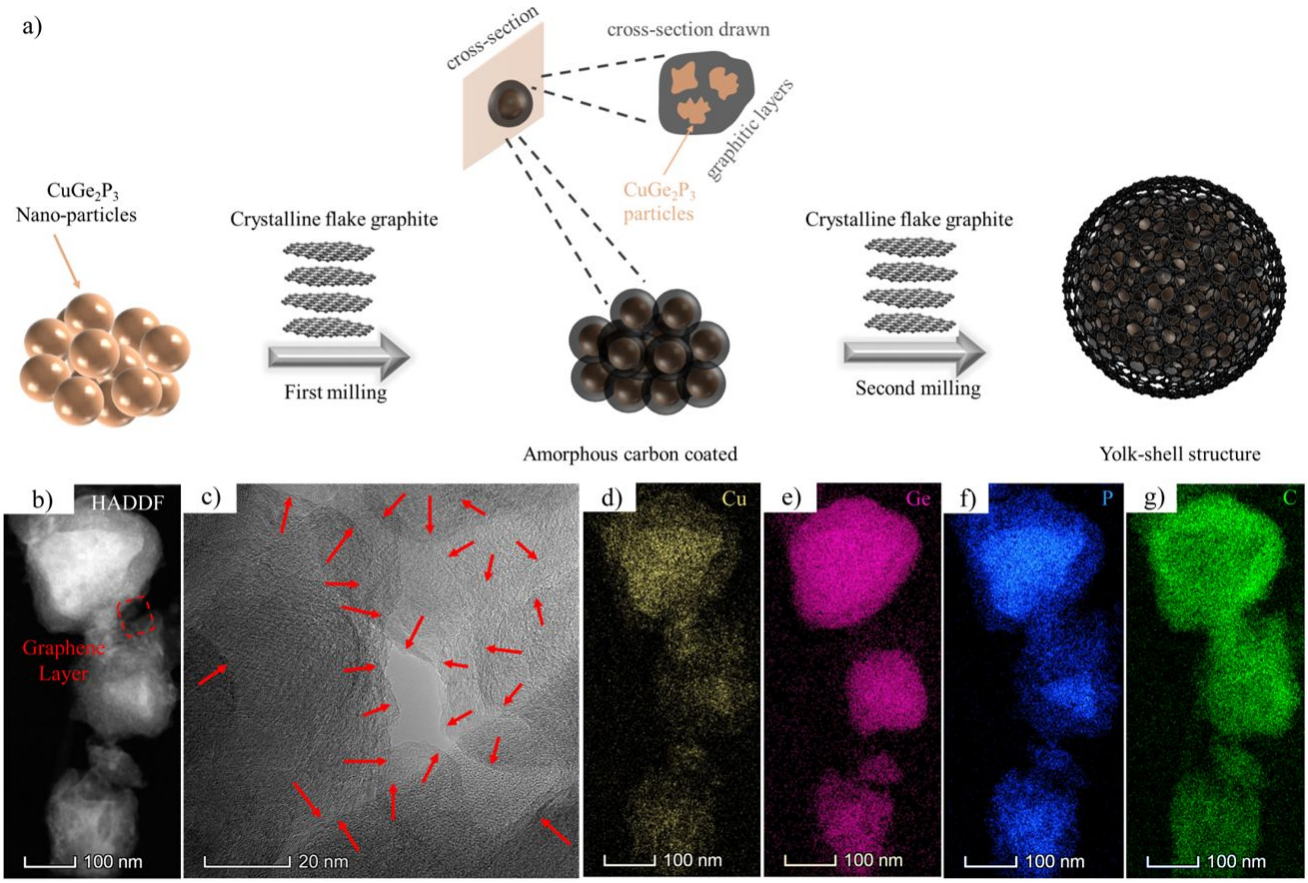

Fig. 5. The synthesis and characterization of the yolk-shell structured amorphous carbon coated $CuGe_2P_3$ nanocomposite: (a) the scheme of the two-stage ball milling processes; (b) low-magnification TEM image; (c) HRTEM images of the marked red rectangle in (b); (d-g) Elemental mapping.

To achieve the long-term cycling stability to the practical level, we construct the yolk-shell structured amorphous carbon coated $CuGe_2P_3$ nanocomposite ($CuGe_2P_3$/C@Graphene) by a two-step mechanical ball milling the lab-prepared $CuGe_2P_3$ with low-cost layered graphite, as illustrated in **Fig. 5a**. In the first step, the particle size of the $CuGe_2P_3$ was significantly decreased into less than five nanometres and embedded into amorphous carbon (**Fig. S20**) produced by the destroyed layered graphite during the high-energy ball milling process. In the second ball milling process, equal amount of layered graphite was poured into the above amorphous carbon coated $CuGe_2P_3$. After a further short milling time of 0.5 h, $CuGe_2P_3$/C@Graphene was formed. As shown in **Fig. S21**, the carbon content in the composite electrode is 22.69%, which is consistent with the predetermined weight ratio of graphite to $CuGe_2P_3$ (2:7 or 22.2% graphite). The elemental mapping images (**Fig. 5d-5g** and **Fig. S22**) further demonstrate the morphology and distribution of $CuGe_2P_3$ within the carbon shell. As taken HRTEM image shown in **Fig. 5c** on the carbon shell, we observed the d-spacing of about 0.33 nm, corresponded to the above-mentioned graphite sheets. The amorphous carbon matrix serves to activate and stabilize the interior of the composite, while the graphite sheets protect and restrains the exterior surface.[48] Benefiting from the

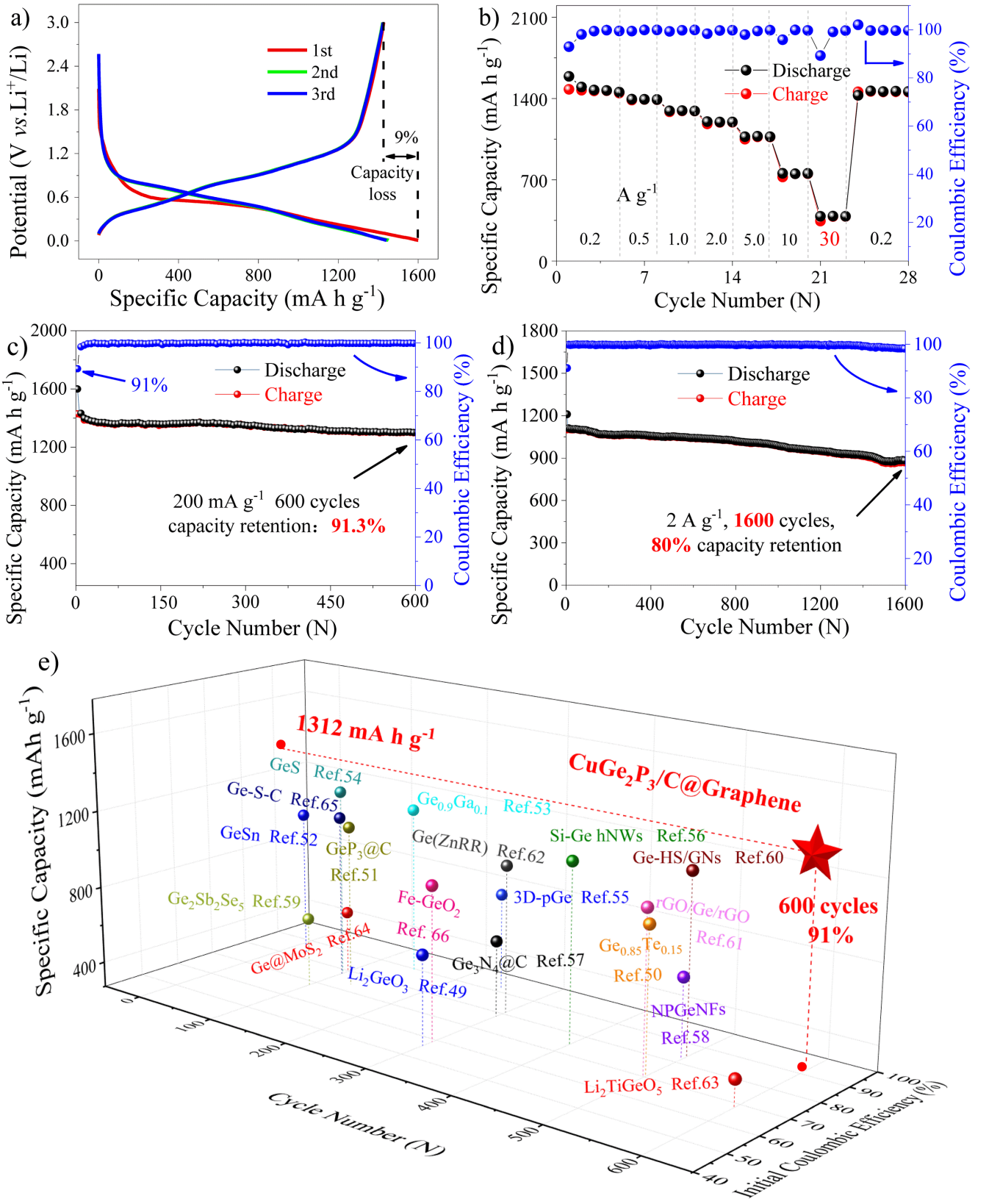

Fig. 6. Electrochemical Li-storage performances of the $CuGe_2P_3$/C@Graphene: (a) first three discharge-charge profiles; (b) rate performance. (c) cycling stability at 200 mA g^{-1}; (d) cycling stability at 2 A g^{-1}; and (e) performances comparisons of the yolk-shell structured amorphous carbon coated $CuGe_2P_3$ nanocomposite ($CuGe_2P_3$/C@Graphene) with recently reported Ge-based anodes in the light of first Coulombic efficiency and long cycling stability.

synergistic combination of these two carbon components, $CuGe_2P_3$/C@Graphene achieved extremely stable cycling stability as well as outstanding rate performance. Such a morphology is also favorable when applied in batteries as the primary nanoparticles can promote the contact between the active materials and electrolytes, and reduce the Li-ionic diffusion path, while the secondary microsized particles can enhance the electrode density, which favors to obtain high volumetric energy density. When applied $CuGe_2P_3$/C@Graphene as anode materials for LIBs, the first three discharge-charge profiles (**Fig. 6a**) are well-matched with the pure cation-disordered $CuGe_2P_3$ compound counterparts (**Fig. 2d**). Moreover, the $CuGe_2P_3$/C@Graphene presents 1,312 mA h g^{-1} capacity after 600 cycles with Coulombic efficiency of approaching to 100% at 0.2 A g^{-1} as shown in **Fig. 6c** and **Fig. S23**, and the remained capacity is 91.3% of the initial charge capacity, thus suggesting its excellent cycling stability. Compared with the fresh $CuGe_2P_3$ electrode, the composite electrode (with carbon) showed slightly lower initial Coulombic efficiency, which can be attributed to the slightly increased specific surface area (**Fig. S24**) and solid electrolyte interface (SEI). At 2 A g^{-1}, the $CuGe_2P_3$/C@Graphene delivers 876 mA h g^{-1} capacity after 1,600 cycles with the remaining capacity ratio up to 80%, suggesting its robust cycling stability, as presented in **Fig. 6d**. When evaluated in rate performance (**Fig. 6b**), the $CuGe_2P_3$/C@Graphene still shows 1464, 1392, 1287, 1167, 1068, 784 mA h g^{-1} with in the ever-increasing current density from 0.2 A g^{-1} to 10 A g^{-1}. Surprisingly, at 30 A g^{-1}, it still can offer

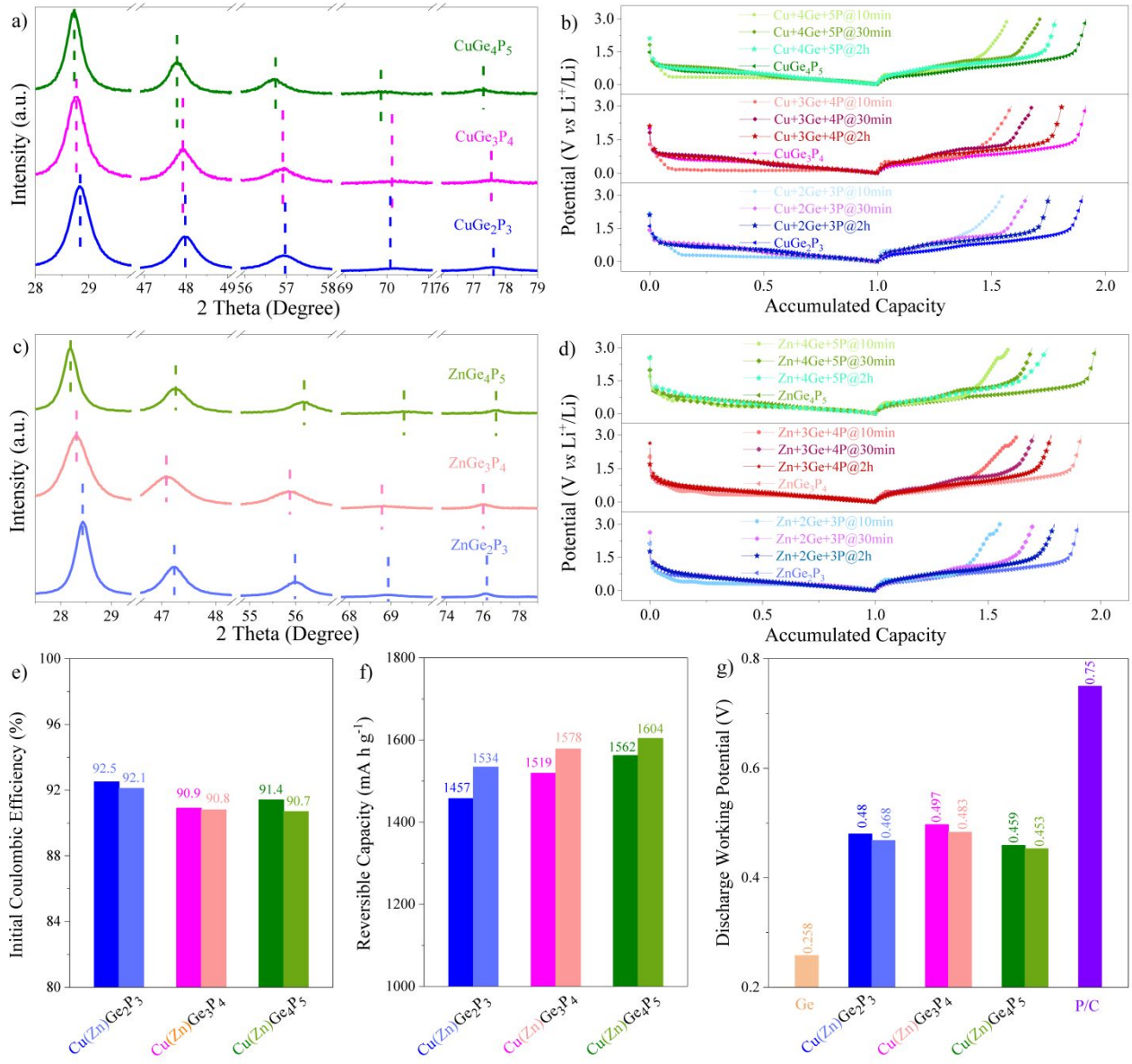

Fig. 7. (a) XRD patterns of cation-disordered Cu-Ge-P series compounds ($CuGe_2P_3$ → $CuGe_3P_4$ → $CuGe_4P_5$); (b) first-cycle galvanostatic discharge-charge profiles of the mechanically milled Cu-Ge-P series compounds at 0.2 A g^{-1}; (c) XRD patterns of cation-disordered Zn-Ge-P series compounds ($ZnGe_2P_3$ → $ZnGe_3P_4$ → $ZnGe_4P_5$); (d) first-cycle galvanostatic discharge-charge profiles of the ball milled Zn-Ge-P samples at 0.2 A g^{-1}; (e-g) initial Coulombic efficiency, reversible capacity and discharge working potential of the cation-disordered Cu(Zn)-Ge-P series compounds.

382 mA h g^{-1} capacity, which is still larger than the theoretical capacity (372 mA h g^{-1}) of the currently utilized graphite anodes. Once the current rate turned back to 200 mA g^{-1}, the initial reversible capacity of 1,457 mA h g^{-1} is also bounce back. These performances shown by $CuGe_2P_3$/C@Graphene anode surpassed most recently reported Ge-based anode materials in terms of long cycling stability, high initial Coulombic efficiency and large remained capacity, as compared in **Fig. 6e** (**Table S5**).[49-66] The ultrahigh performances mainly profit from the following aspects: 1) inherently ultrafast Li-ionic and electronic conductivities of the cation-disordered $CuGe_2P_3$ compound; 2) the reversible Li-storage mechanism along with superior electrochemical intermediates; 3) the bi-carbon protection strategy. To demonstrate the practical application potential of the $CuGe_2P_3$/C@Graphene anodes, we assembled a full cell using a $LiFePO_4$ cathode and our $CuGe_2P_3$/C@Graphene composite anode. Specifically, the anode loading was about 3 mg cm^{-2} and the anode capacity is slightly (1.1 times) larger than the cathode capacity to avoid the lithium dendrite growth. As shown in **Fig. S25**, the full cell can be cycled over 20 cycles without capacity degradation, thus confirming its applicability to practical applications.

Taking the cation-disordered structural flexibility into account, we continue to expand the horizon to contain a new class of cation-disordered Cu(Zn)-Ge-P series compounds based on the $CuGe_2P_3$ case and further evaluate them as anodes for LIBs. First of all, concerning the cation-disordered characteristic of the as-prepared $CuGe_2P_3$, series compounds with various cationic ratios (Cu/Ge ratios) were prepared by the similar ball milling method. As presented in **Fig.7a** and **Fig. S26a**, with the increasing content of Ge locating at the cationic sites of the Cu-Ge-P series compounds, all these Ge-like diffraction peaks ($CuGe_2P_3$ → $CuGe_3P_4$ → $CuGe_4P_5$) only slightly shift to lower angles, suggesting these newly-formed compounds own similar crystal structure, although with a little expansion because of the larger atomic size of Ge compared with that of Cu. Besides, as known, Zn locates at the right side of Cu in the Periodic Table of elements and, furthermore, as a noncompetitive metal with those popular cathodes, it also contributes capacity when applied in LIBs. In the light of above merits and its comparable atomic size, bonding feature and electronegativity to Cu counterparts, we take the place of Cu with Zn to extend the family and simultaneouly alter the cationic ratios of Zn/Ge. Just like we planned, the Zn-Ge-P ($ZnGe_2P_3$ → $ZnGe_3P_4$ → $ZnGe_4P_5$) present similar structural features (**Fig. 7c**, **7d**, and **Fig. S26b**) to the above Cu-Ge-P compounds counterparts. All results suggest these cation-disordered arrangements at the atomic scale seem to involve with homologous atoms in a large range. As known, the micro-structures and components of materials determine their physicochemical properties including the electrochemical performances and in the meanwhile elemental doping can also exert a significant influence on physicochemical properties. Therefore, we further evaluate Li-storage behaviors of the above-prepared Cu(Zn)-Ge-P family compounds. As presented in **Fig. 7e**, **7f**, **7g**, and **Fig. S27**, all the cation-disordered anode materials deliver large reversible capacities between 1,400 mA h g^{-1} and 1,650 mA h g^{-1}(**Fig. 7f**), which are close to their theoretical capacities on the basis of the terminal Li-alloy products of $Li_{3.75}Ge$, Li_3P and LiZn, with high first Coulombic efficiency more than 90% (**Fig. 7e**). More interestingly, all these anodes present an appropriately low and safe working potentials ranging from 0.35 V to 0.55 V vs. Li^+/Li (**Fig. 7g** and **Fig. S28**). All these working potentials are above Li-plating potentials, thus avoiding the growth of Li-dendrites, which impales separators especially at large current rates. These working potentials of the newly formed family anode materials are all appropriately lower than phosphorus carbon composite counterpart, thus realizing higher energy density when served in a full battery. Consequently, we find a new class of cation-disordered Cu(Zn)-Ge-P electrode candidate materials with more practical potentials, which fills the gap between Ge and P anodes, thus simultaneously meeting the standards of high safety as well as high-energy density when served in a full battery.

In conclusion, we have prepared a cation-disordered $CuGe_2P_3$ compound by a simple and scalable mechanical ball milling process and demonstrated its ultrahigh performances as an advanced anode material for LIBs. The superior performance can be attributed to its Li-inert Cu constituent[67] and stronger resistance against volume variation during cycling, as validated by first-principles calculations and experiment measurements. The cation-disordered $CuGe_2P_3$ experienced a reversible Li-storage mechanism of conversion reaction, as revealed by various characterizations including the ex-situ high-resolution synchrotron X-ray diffraction, XRD, HRTEM along with SAED, XPS, and Raman spectroscopy. When hybridized with graphite, the constructed $CuGe_2P_3$/C@Graphene offers a reversible capacity of 1,464 mA h g^{-1} with an initial Coulombic efficiency up to 91% and still remained 1,312 mA h g^{-1} capacity after 600 cycles at a current rate of 0.2 A g^{-1}. When cycled at 2 A g^{-1}, a reversible capacity of 876 mA h g^{-1} was still retained after 1,600 cycles. Further, remarkable rate performance has also been demonstrated; the composite delivered up to 384 mA h g^{-1} capacity at an ultrahigh current of 30 A g^{-1}. The above Li-storage performances surpass most Ge-based anodes ever reported. Moreover, it is found that a class of novel cation-disordered Cu(Zn)-Ge-P compounds with different cation ratios can be prepared by the same method, which have shown similar performance: large reversible capacities, high initial Coulombic efficiency, suitable operating potentials, and enhanced safety and energy density. These electrode materials are promising to be the next-generation anode materials with ultrahigh performances.

Experimental Section

Material preparation

As a typical synthesis procedure, red P, Cu and Ge powders in a molar ratio of 3:1:2 was completely mixed by virtue of a planetary mechanical ball milling at 400 rpm for a certain number of hours in argon to obtain pure cation-disordered $CuGe_2P_3$ powders. Stainless steel tank of 300 ml along with stainless steel hard alloy balls of Φ5 mm were utilized for mechanical ball milling. The mass ratio of grinding balls to raw materials was 20:1. For $CuGe_2P_3$/C@Graphene nanocomposite (weight ratio of C: $CuGe_2P_3$ is 2:7), a two-stage ball milling processes were carried out. Firstly, one half of the required graphite was poured and grinded with the lab-prepared $CuGe_2P_3$ for 10 h to achieve the well encapsulating of $CuGe_2P_3$. Then, the other half of the required graphite was poured and reground for another 1 h to enhance the electronic conductivity of the nanocomposite. Other cation-disordered Cu(Zn)-Ge-P compounds were prepared under similar mechanical ball milling experimental conditions.

Material characterization

We characterized the as-synthesized samples using X-ray diffraction (XRD, Bruker D8 ADVANCE) and Raman spectrometer (HORIBA Jobin Yvon*/LabRAM HR Evolution) with a 532 nm excitation laser. We investigated crystalline structure of the as-prepared samples further utilizing synchrotron radiation source (λ= 0.2362 Å) at Beamline 28-ID-2 at National Synchrotron Light Source II (NSLS-II) at Brookhaven National Laboratory, Upton, NY. We observed morphologies and microstructures of the as-prepared samples applying a field-emission scanning electron microscope (FESEM, Hitach SU8220) and a high-resolution field-emission transmission electron microscope (HRTEM, FEI, Thermo Talos F200S) as well as an ASAP 2460 Surface Area Analyzer, respectively. We obtained X-ray photoelectron spectroscopy (XPS) data by Thermo Fisher Escalab 250Xi electron spectrometer. We collected the data about the thermal stability by High temperature synchronous analyzer (TGA/DSC3+, Switzerland).

Electrochemical characterization

We fabricated pure phase Cu(Zn)-Ge-P electrode films by virtue of coating the slurry of 70 wt.% active materials, 10 wt.% Li-PAA binder and 20 wt.% carbon black as electronic conductivity agent on a current collector of Cu foil and then drying at 70 ^oC overnight under vacuum. For $CuGe_2P_3$/C@Graphene and cation-disordered $CuGe_2P_3$ samples, we prepared electrode films by virtue of only coating the slurry containing 90 wt.% active materials, and 10 wt.% Li-PAA binder on current collector of Cu foil without using any conductive agents. We assembled CR2032 coin-type cells in a glove box filled with Ar (H_2O < 0.03 ppm, O_2 < 0.05 ppm, Mbraun, Labmaster 130) using Li metal as both counter and reference electrodes, 1 M $LiPF_6$ in EC/DEC/EMC (1:1:1 by volume) as electrolytes, and Celgard 2325 as separators. The areal mass loading was about 1-1.5 mg cm^{-2}. We conducted electrochemical tests applying a LAND battery tester (Wuhan Kingnuo Electronic Co., China), a battery testing system (Hokuto Denko, HJ1001SD8) and electrochemical workstation (Autolab, Pgstat 302N). In addition, electrochemical impedance spectroscopy (EIS) tests were carried out in a frequency range from 100 kHz to 0.01 Hz. All tests were performed at a constant temperature of 25 ^oC. The gravimetric specific capacity was evaluated based on the mass of active materials.

Calculations detail

We performed theoretical calculations applying Vienna Ab-initio Simulation Package (VASP).[68,69] We applied the exchange correlation functional with generalized gradient approximation proposed by Perdew, Burke and Ernzerhof. The inner core-electrons were frozen by virtue of projector augmented wavefunction, with outer valence electron configuration for P $3s^23p^3$, Ge $3d^{10}4s^24p^2$, Cu $3d^{10}4s^1$. We utilized the 4x4x4 Monkhorst-Pack reciprocal grid, accompanying with 400 eV energy cut off serving as sufficient energy calculations. We also applied Gaussian smearing with smearing width (0.05 eV) to speed up computation of electronic energy close to Fermi level.

Conflicts of interest

There are no conflicts to declare.

Acknowledgements

This work was supported by the National Natural Science Foundation of China (No. 21701030), and US National Science Foundation (DMR-1742828). All authors acknowledged facilities applications of Georgia Institute of Technology, Guangdong University of Technology as well as National Taiwan Normal University.

References

1. K. H. Seng, M. H. Park, Z. P. Guo, H. K. Liu and J. Cho, *Angew. Chem.*, 2012, **51**, 5657-5661.
2. X. Wang, L. Fan, D. Gong, J. Zhu, Q. Zhang and B. Lu, *Adv. Funct. Mater.*, 2016, **26**, 1104-1111.
3. H. Kim, Y. Son, J. Lee, M. Lee, S. Park, J. Cho and H. C. Choi, *Chem. Mater.*, 2016, **28**, 6146-6151.
4. M. H. Seo, M. Park, K. T. Lee, K. Kim, J. Kim and J. Cho, *Energy Environ. Sci.*, 2011, **4**, 425-428.
5. Q. Ai, Q. Fang, J. Liang, X. Xu, T. Zhai, G. Gao, H. Guo, G. Han, L. Ci and J. Lou, *Nano Energy*, 2020, **72**, 104657.
6. Y. Sun, S. Jin, G. Yang, J. Wang and C. Wang, *ACS Nano*, 2015, **9**, 3479-3490.
7. C. Yan, W. Xi, W. Si, J. Deng and O. G. Schmidt, *Adv. Mater.*, 2013, **25**, 539-544.
8. S. Liu, J. Feng, X. Bian, Y. Qian, J. Liu and H. Xu, *Nano Energy*, 2015, **13**, 651-657.
9. H. Kim, Y. Son, C. Park, J. Cho and H. C. Choi, *Angew. Chem.*, 2013, **52**, 5997-6001.
10. D. Li, H. Wang, H. K. Liu and Z. Guo, *Adv. Energy Mater.*, 2016, **6**, 1501666.
11. Y. Chen, C. Yan and O. G. Schmidt, *Adv. Energy Mater.*, 2013, **3**, 1269-1274.
12. C. Kim, G. Song, L. Luo, J. Y. Cheong, S. H. Cho, D. Kwon, S. Choi, J. W. Jung, C. M. Wang, I. D. Kim and S. Park, *ACS Nano*, 2018, **12**, 8169-8176.

13. A. C. Serino, J. S. Ko, M. T. Yeung, J. J. Schwartz, C. B. Kang, S. H. Tolbert, R. B. Kaner, B. S. Dunn and P. S. Weiss, *ACS Nano*, 2017, **11**, 7995-8001.
14. X. Li, Z. Yang, Y. Fu, Li Qiao, D. Li, H. Yue and D. He, *ACS Nano*, 2015, **9**, 1858-1867.
15. J. Ryu, J. H. Seo, G. Song, K. Choi, D. Hong, C. Wang, H. Lee, J. H. Lee and S. Park, *Nat. Commun.*, 2019, **10**, 2351.
16. K. C. Klavetter, J. P. d. Souza, A. Hellera and C. B. Mullins, *J. Mater. Chem. A*, 2015, **3**, 5829-5834.
17. P. R. Abel, K. C. Klavetter, K. Jarvis, A. Heller and C. B. Mullins, *J. Mater. Chem. A*, 2014, **2**, 19011-19018.
18. T. Li, C. Lim, Y. Cui, X. Zhou, H. Kang, B. Yan, M. L. Meyerson, J. A. Weeks, Q. Liu, F. Guo, R. Kou, Y. Liu, V. D. Andrade, F. D. Carlo, Y. Ren, C. J. Sun, C. B. Mullins, L. Chen, Y. Fu and L. Zhu, *J. Mater. Chem. A*, 2020, **8**, 750-759.
19. P. R. Abel, K. C. Klavetter, A. Heller and C. B. Mullins, *J. Phys. Chem. C*, 2014, **118**, 17407-17412.
20. P. R. Abel, A. M. Chockla, Y. M. Lin, V. C. Holmberg, J. T. Harris, B. A. Korgel, A. Heller and C. B. Mullins, *ACS Nano*, 2013, **7**, 2249-2257.
21. W. Xiao, J. Zhou, L. Yu, D. Wang and X. W. Lou, *Angew. Chem.*, 2016, **55**, 7427-7431.
22. C. C. Li, B. Wang, D. Chen, L. Y. Gan, Y. Zhang, Y. Yang, H. Geng, X. Rui and Y. Yu, *ACS Nano*, 2020, **14**, 531-540.
23. D. Duveau, B. Fraisse, F. Cunin and L. Monconduit, *Chem. Mater.*, 2015, **27**, 3226-3233.
24. N. Bensalah, M. Matalkeh, N. K. Mustafa and H. Merabet, *Phys. Status Solidi A*, 2020, **217**, 1900414.
25. W. Li, H. Li, Z. Lu, L. Ke, L. Gan, T. Zhai and H. Zhou, *Energy Environ. Sci.*, 2015, **8**, 3629-3636.
26. W. Li, X. Li, J. Yu, J. Liao, B. Zhao, L. Huang, A. Abdelhafiz, H. Zhang, J. H. Wang, Z. Guo and M. Liu, *Nano Energy*, 2019, **61**, 594-603.
27. D. Kim, K. Zhang, M. Cho and Y. M. Kang, *Energy Environ. Sci.*, 2019, **12**, 1326-1333.
28. J. H. Kim, J. H. Yun and D. K. Kim, *Adv. Energy Mater.*, 2018, **8**, 1703499.
29. Y. Wei, L. Huang, J. He, Y. Guo, R. Qin, H. Li and T. Zhai, *Adv. Energy Mater.*, 2018, **8,** 1703635.
30. J. R. Rodriguez, Z. Qi, H. Wang, M. Y. Shalaginov, C. Goncalves, M. Kang, K. A. Richardson, J. G. Sanchez, M. G. M. Armenta and V. G. Pol, *Nano Energy*, 2020, **68**, 104326.
31. Y. Wei, L. Huang, J. Chen, Y. Guo, S. Wang, H. Li and T. Zhai, *ACS Appl. Mater. Interfaces*, 2019, **11**, 41374-41382.
32. M. Li, Z. Zhang, X. Ge, Z. Wei, Y. Yao, H. Chen, C. Wang, F. Du and G. Chen, *Chem. Eng. J.*, 2018, **331**, 203-210.
33. S. Yuvaraj, K. Karthikeyan and R. K. Selvan, *J. Colloid Interface Sci.*, 2017, **498**, 76-84.
34. G. H. Lee, M. C. Sung, J. C. Kim, H. J. Song and D. W. Kim, *Adv. Energy Mater.*, 2018, **8**, 1801930.
35. L. Fu, X. Zheng, L. Huang, C. Shang, K. Lu, X. Zhang, B. Wei and X. Wang, *Nanoscale Res. Lett.*, 2018, **13**, 193.
36. J. Zhou, W. Zhang, H. Zhao, J. Tian, Z. Zhu, N. Lin and Y. Qian, *ACS Appl. Mater. Interfaces*, 2019, **11**, 22371-22379.
37. T. He, J. Feng, Y. Zhang, L. Zu, G. Wang, Y. Yu and J. Yang, *Adv. Energy Mater.*, 2018, **8**, 1702805.
38. L. Fu, C. Shang, J. Ma, C. Zhang, X. Zang, J. Chai, J. Li and G. Cui, Sci. *China-Mater.*, 2018, **61**, 1177-1184.
39. Y. Fu, Q. Wei, G. Zhang and S. Sun, *Adv. Energy Mater.*, 2018, **8**, 1702849.
40. W. Liu, H. Zhi and X. Yu, *Energy Storage Mater.*, 2019, **16**, 290-322.
41. W. Li, X. Li, J. Liao, B. Zhao, L. Zhang, L. Huang, G. Liu, Z. Guo and M. Liu, *Energy Environ. Sci.*, 2019, **12**, 2286-2297.
42. O. Crosnier, C. Mounsey, P. S. Herle, N. Taylor and L. F. Nazar, *Chem. Mater.*, 2003, **15**, 4890-4892.
43. S. Wenzel, S. Randau, T. Leichtweiß, D. A. Weber, J. Sann, W. G. Zeier, and J. Janek, *Chem. Mater.*, 2016, **28**, 2400-2407.
44. N. Wu, Y. Li, A. Dolocan, W. Li, H. Xu, B. Xu, N. S. Grundish, Z. Cui, H. Jin, and J. B. Goodenough, *Adv. Funct. Mater.,* 2020, **30**, 2000831.
45. G. K. Dey, R. T. Savalia, S. K. Sharma and S. K. Kulkarni, *Corrosion Sci.*, 1989, **29**, 823-831.
46. W. Li, J. Yu, J. Wen, J. Liao, Z. Ye, B. Zhao, X. Li, H. Zhang, M. Liu and Z. Guo, *J. Mater. Chem. A*, 2019, **7**, 16785-16792.
47. S. Lebègue and O. Eriksson, Phys. Rev. B, 2009, **79**, 115409.
48. T. Wang, K. Zhang, M. Park, V. W. H. Lau, H. Wang, J. Zhang, J. Zhang, R. Zhao, Y. Yamauchi and Y. M. Kang, *ACS Nano*, 2020, **14**, 4352-4365.
49. M. M. Rahman, I. Sultana, T. Yang, Z. Chen, N. Sharma, A. M. Glushenkov and Y. Chen, *Angew. Chem.*, 2016, **55**, 16059-16063.
50. Z. Yu, L. Yuan, Y. Wei, H. Li, X. Meng, Y. Li and F. Endres, *Chem. Commun.*, 2019, **55**, 10412-10415.
51. W. Qi, H. Zhao, Y. Wu, H. Zeng, T. Tao, C. Chen, C. Kuang, S. Zhou and Y. Huang, *Sci. Rep.*, 2017, **7**, 43582.
52. J. Doherty, S. Biswas, D. McNulty, C. Downing, S. Raha, C. O'Regan, A. Singha, C. O'Dwyer and J. D. Holmes, *Chem. Mater.*, 2019, **31**, 4016-4024.
53. E. J. Powell, S. M. Wood, H. Celio, A. Heller and C. B. Mullins, *J. Mater. Chem. A*, 2015, **3**, 23442-23447.
54. Y. J. Cho, H. S. Im, H. S. Kim, Y. Myung, S. H. Back, Y. R. Lim, C. S. Jung, D. M. Jang, J. Park, E. H. Cha, W. I. Cho, F. Shojaei and H. S. Kang, *ACS Nano*, 2013, **7**, 9075-9084.
55. T. Yoon, G. Song, A. M. Harzandi, M. Ha, S. Choi, S. Shadman, J. Ryu, T. Bok, S. Park and K. S. Kim, *J. Mater. Chem. A*, 2018, **6**, 15961-15967.
56. K. Stokes, G. Flynn, H. Geaney, G. Bree and K. M. Ryan, *Nano Lett.*, 2018, **18**, 5569-5575.
57. C. Kim, G. Hwang, J. W. Jung, S. H. Cho, J. Y. Cheong, S. Shin, S. Park and I. D. Kim, *Adv. Funct. Mater.*, 2017, **27**, 1605975.
58. C. Kim, G. Song, L. Luo, J. Y. Cheong, S. H. Cho, D. Kwon, S. Choi, J. W. Jung, C. M. Wang, I. D. Kim and S. Park, *ACS Nano*, 2018, **12**, 8169-8176.
59. J. R. Rodriguez, Z. Qi, H. Wang, M. Y. Shalaginov, C. Goncalves, M. Kang, K. A. Richardson, J. G. Sanchez, M. G. M. Armenta and V. G. Pol, *Nano Energy*, 2020, **68**, 104326.
60. R. Mo, D. Rooney and K. Sun, *Energy Storage Mater.*, 2020, **26**, 414-422.
61. B. Wang, J. Jin, X. Hong, S. Gu, J. Guo and Z. Wen, *J. Mater. Chem. A*, 2017, **5**, 13430-13438.

62. S. Choi, Y. G. Cho, J. Kim, N. S. Choi, H. K. Song, G. Wang and S. Park, *Small*, 2017, **13**, 1603045.
63. Y. Liu, Q. Bai, A. M. Nolan, Y. Zhou, Y. Wang, Y. Mo and Y. Xia, *Nano Energy*, 2019, **66**, 104094.
64. M. H. Hsieh, G. A. Li, W. C. Chang and H. Y. Tuan, *J. Mater. Chem. A*, 2017, **5**, 4114-4121.
65. G. K. Sung and C. M. Park, *J. Mater. Chem. A*, 2017, **5**, 5685-5689.
66. J. Wu, N. Luo, S. Huang, W. Yang and M. Wei, *J. Mater. Chem. A*, 2019, **7**, 4574-4580.
67. M. N. Obrovac, L. Christensen, D. B. Le and J. R. Dahn, *J. Electrochem. Soc.*, 2007, **154**, A849-A855.
68. J. D. Pack and H. J. Monkhorst, *Phys. Rev. B*, 1977, **16**, 1748-1749.
69. G. Kresse and D. Joubert, *Phys. Rev. B*, 1999, **59**, 1758-1775.